A 6 x 30 Gb/s tunable transmitter PIC with low RF crosstalk from an open-access InP foundry

A 6 x 30 Gb/s Tunable Transmitter PIC with low RF Crosstalk from an Open-Access InP Foundry

Weiming Yao, *Member, IEEE,* Barry Smalbrugge, Meint K. Smit, *Fellow, IEEE,* Kevin A. Williams, *Member, IEEE,* and Michael J. Wale, *Member, IEEE*

***Abstract*—We demonstrate a six-channel tunable optical transmitter photonic integrated circuit (PIC) fabricated in an open-access indium phosphide foundry process. The device monolithically integrates 20 nm tunable lasers and 30 Gb/s Mach-Zehnder modulators, without the use of Bragg gratings or quantum wells for phase modulation, to form a compact $3.9 \times 4.5\mathrm{mm}^2$ high-density 6×30 Gb/s parallel transmitter. It exhibits a capacity density metric of 10 Gb/s/mm^2, comparable to state-of-the-art results from literature and low < -50 dB inter-channel radio-frequency crosstalk. With an attractive price point of 7 USD/Gb/s the device can be a low-cost solution for data center interconnect or residential access networks.**

***Index Terms*—Integrated Photonics, WDM Transmitter, Integrated Optics, Photonic Integrated Circuits, Tunable Transmitter**

I. Introduction

The steady growth of data traffic in recent years poses many technical and economical challenges on optical transport hardware, especially in data center and residential access networks, where it is expected of optical transceivers to steadily increase their capacity but reduce in cost and footprint.

Standard interfaces such as 100 Gb Ethernet with 4 parallel lanes at 25 Gb/s have been readily accepted for pluggable small form-factor modules whereas work is already ongoing to define the next generation interface for 400 Gb Ethernet [1]. C-band wavelength-division multiplexing (WDM) has also been suggested as a potential concept to incorporate more wavelength channels in the system compared to conventional standards at 1.3 μm wavelength [2]. Likewise, for residential access, WDM passive optical networks (PON) using transmitters at 10 Gb/s or scaled-up 25 Gb/s line rates are envisioned for NG-PON2 [3], [4]. Here, wavelength tunability is preferred to allow for flexible network control and provisioning [5], but need to be available at an affordable price range [6]. Common transmitter systems based on gratings in combination with Mach-Zehnder modulators (MZM) can offer tens of nanometers of tuning but meeting cost requirements is challenging [7]. This points to the need for high volume, low-cost, tunable, high-capacity WDM transmitters which will be attractive to both datacenter interconnect and residential access networks.

Photonic integrated circuits (PIC) technology is ideal for realizing such parallel WDM transmitters as multiple wavelength channels can be densely integrated on the same chip. The generic foundry model for photonic integration [8] has made the technology more accessible to everyone, resulting in open-access indium phosphide [9] and silicon material platforms [10]. Monolithic integration of laser arrays with modulators and passive components on indium phosphide is a mature and established technology that can realize large-scale parallel transmitters on a single compact chip [11], [12] without the need for hybrid assembly with lasers, required for silicon photonics. Costs can be kept low through the generic foundry model where standardized processes are capable of producing high-capacity WDM transmitters [13]. Two of the most recent transmitter PIC examples fabricated in generic InP foundries are both aimed at the data center and residential access application space, making use of 8 WDM channels [14], [15]. Although realized on two separate generic platforms, each offering their own building blocks, both transmitters resemble each other in their parallel architecture with multiple channels. This can be viewed as foundry interoperability on a functional level which becomes commercially important when second sourcing in the production process is required. By properly combining basic foundry and custom building blocks, the same functionality, in this case parallel tunable WDM transmitters, can be achieved on different InP foundries.

In this work, we present a device fabricated in one of the JePPIX[1] platforms using a general-purpose open-access process, characterized by its low-complexity and single-regrowth active-passive integration scheme [16]. Compared to the two other platforms [14], [15] it can offer tunable WDM transmitter fabrication at lower cost due to its simpler process. We have previously demonstrated that such a technology can realize tunable lasers and modulators for 10 Gb/s applications without the need of Bragg gratings or additional quantum well regrowths [17]. Optimization of the modulator design can further improve the line rate and we have presented initial results of a six channel 6 x 30 Gb/s tunable transmitter realized on the same platform [18]. This proof-of-concept demonstrates the capabilities of such a low-complexity process with respect to speed and density. It can serve 25 Gb/s WDM PON applications or provide a cost-effective solution for IEEE 25GBASE and a testbed for 200 Gb Ethernet and beyond.

In this paper we discuss the device from [18] in more detail by elaborating on the specific laser and modulator design and showing extended characterization results of components, including bit error rate and RF crosstalk measurements using a custom test assembly. In section II, we first describe the InP platform and how the building block approach is used within the foundry model to establish the transmitter PIC. Measurement results on the DC and dynamic performance of the fabricated PIC are presented in section III whereas section IV deals with the performance after placing it in a PCB test assembly. The latter allows to test simultaneous channel

[1]Joint European Platform for Photonic Integrated Components and Circuits

operation and the evaluation of RF crosstalk effects. Finally, section IV discusses bandwidth density metrics and section V summarizes the paper.

II. Platform Technology and Building Blocks

We chose to realize the transmitter PIC in an InP foundry platform as described in [16] due it's mature technology and well-established process design kit (PDK). The integration of active and passive waveguides follows a butt-joint integration scheme, where the active stack consisting of quantum wells at 1550 nm are first grown with MOCVD. Active areas are masked and the rest is etched away. A transparent passive layer for waveguides is then re-grown to match the height of the active layer. A subsequent overgrowth step covers the entire wafer with the p-doped upper cladding. Details of a similar process are reported in [19]. It offers the full palette of lasers, modulators, detectors and passive components. The PDK defines basic building blocks such as optical amplifiers, phase sections, passive waveguides, splitters and combiners [9]. More complex composite building blocks are formed through the combination of basic blocks or addition of custom designed structures to existing components. Both the tunable laser and traveling-wave modulator used in this work are custom designed composite building blocks.

A. Tunable Coupled-Cavity Laser

The design of the laser is based on a previous device that was reported in [20], [21], consisting of two linear cavities that are coupled together by a special multi-mode interference reflector (MIR) [22]. One of the two cavities has an additional Michelson-Interferometer (MI) filter built-in which can be tuned in its spectral response by reverse biased phase shifters to increase the wavelength tuning range. The structure of the laser is schematically shown in Fig. 1. Cavity 1 and 2 are formed through special MIRs R2, R3 and the normal MIR R1 [23] and R2, respectively. The MI contains two arms with different path lengths, resulting in a wavelength dependent reflection response. The special MIR R3 is used to close the interferometer and suppresses every second FSR of the MI response due to its custom designed phase relation [21]. Each cavity contains passive waveguides, a current injection phase tuning (ϕ) and a gain section. The former is constituted of a quaternary InGaAsP (λ_g =1.25 µm) core layer between p-InP and n-InP cladding layers whereas the latter contains active multi-quantum wells (λ_g =1.55 µm) in the core region.

Lasing is achieved by biasing both gain sections above threshold and wavelength tuning by utilizing the Vernier effect through a combination of cavity mode tuning using the phase sections and its interplay with the MI filter response [21]. It has been shown that this concept can yield 25 nm of tuning range [17]. Fig. 2 depicts the wavelength tuning of a laser in this work, where a tuning set is a combination of MI voltage and phase current values that lead to a specific output wavelength. The voltage on each arm of the MI is denoted with V_1 and V_2 respectively. One arm is biased during the first 10 nm of wavelength tuning and the second arm is used for the subsequent 10 nm. Here, only one of the two phase sections

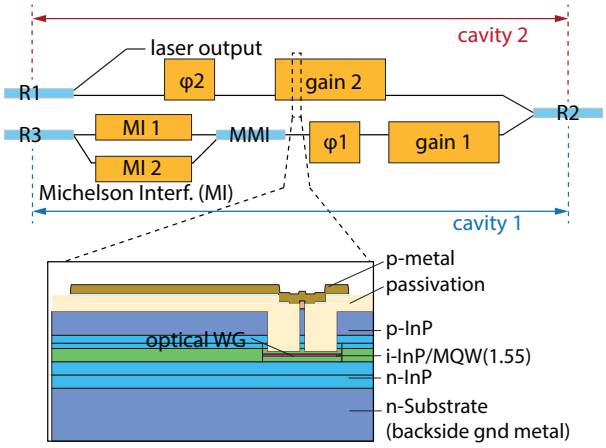

Fig. 1: Schematic of the coupled-cavity tunable laser with intra-cavity Michelson interferometer (MI) and a cross section through the active section of the generic foundry platform.

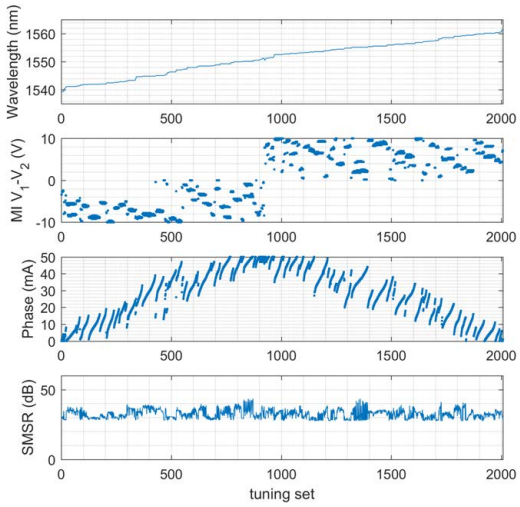

Fig. 2: Tuning map of the coupled-cavity laser. A tuning set denotes the combination of MI voltage and phase current values, resulting in a specific laser wavelength. A tunability of 20 nm can be achieved.

was used in operation due to the limitations of probing needles in the setup. This explains the occurrence of small jumps in the wavelength plot. Up to 20 nm of tuning range can be achieved. The previous design [17] has been adapted with respect to cavity lengths in order to properly fit the laser array into the transmitter footprint, resulting in a slightly lower tuning range. Furthermore, we improved on the layout by introducing a horizontal offset between the gain sections of both cavities. This decouples the heat spread of both and reduces the thermal roll-off effect, identified as a limiting factor in the LI curve from the previous work.

This laser design has the advantage of wide tunability without the need of a grating process that requires e.g. slow and costly electron-beam lithography, and can be manufactured in the low-complexity generic foundry process.

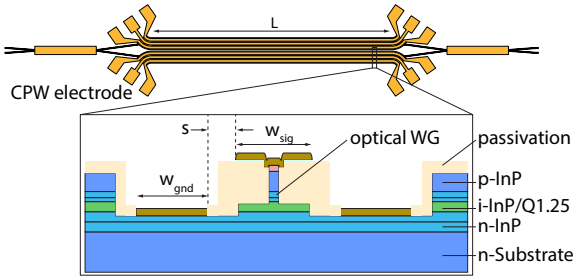

Fig. 3: Schematic of the dual-drive Mach-Zehnder modulators with the cross section of the passive sections in the generic foundry platform.

B. Traveling-Wave Modulator

The modulators utilized in this work are based on coplanar traveling-wave electrodes that are custom designed on the foundry platform to form a Mach-Zehnder modulator in dual-drive mode. Fig. 3 shows the modulator structure with the underlying waveguide cross section. A coplanar waveguide configuration is used around the optical waveguide so that the modulating electrical field can build up along the p-i-n waveguide junction. Here we utilize electro-optic effects in the bulk Q1.25 core material to induce an index change. Although not as efficient as state-of-the-art quantum well modulators based on quantum-confined stark effect, the approach here omits an additional regrowth step and therefore reduces the fabrication complexity and cost.

The coplanar modulator electrode is well known to exhibit low characteristic impedance (25-35 Ohm) [24] due to the constraints of the optical waveguide geometry and the attenuation limits imposed by the doped semiconductors. We simulated the microwave attenuation and characteristic impedance using a commercial 3D EM solver (CST MWS) and plot the results in Fig. 4. It can be seen that the impedance increases with the distance between ground and signal electrode. However, the attenuation grows similarly as the electric field penetrates more lossy semiconductor material. We chose a signal-ground separation of 10 µm as a good trade-off between impedance match and low attenuation. The signal electrode width was chosen to be 10 µm to reduce on the one hand the parasitic capacitance between it and the ground n-InP layer as discussed in [25] and on the other hand to be sufficiently wide to yield a low resistance conductor. The ground electrode width was chosen to be 10 µm as well to increase as much as possible the characteristic impedance. To verify the modeling results, different long modulator electrodes have been fabricated and the line impedance extracted from two-port S-parameter measurements following the de-embedding strategy in [26]. This leads to an impedance value of 33 Ω at 10 GHz as shown in Fig. 5. The length of the phase shifters is 1.25 mm which has been determined as a good compromise between modulator bandwidth and efficiency.

Both the tunable laser and the modulator are composite building blocks and are connected with each other to form a tunable transmit channel. The next section details how the parallel transmitter PIC is formed from these tunable channels and presents its static and dynamic characteristics.

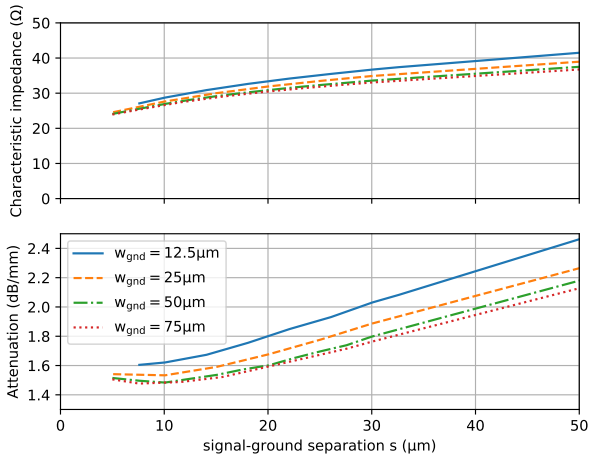

Fig. 4: Simulated characteristic impedance and microwave attenuation at 10 GHz as a function of separation s between signal and ground electrodes of the modulator with different ground width values.

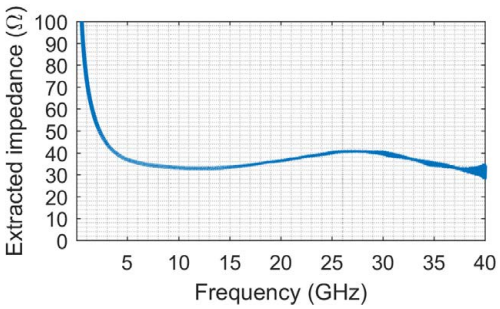

Fig. 5: Extracted characteristic impedance from S-parameter measurements of phase shifters show 33 Ω at 10 GHz.

III. Chip-Level Performance

The architecture of the transmitter PIC is layed out in Fig. 6 and shows how the single channel consisting of laser and modulator is scaled to the parallel transmitter fitting into a 3.9 x 4.5 mm^2 chip area. Both the tunable laser and the traveling-wave modulator are elongated in the horizontal direction and occupy little space in the vertical direction so that the chip area can be efficiently utilized to include six channels. Two arrayed-waveguide gratings (AWG) are used to perform wavelength multiplexing of three channels each and a MMI coupler combines them into a final output waveguide. Next free-spectral-range ports of the AWGs are used for test and monitoring purposes. To boost the signal output power and partially overcome the AWG losses, semiconductor optical amplifiers (SOAs) are integrated into each channel. Fig. 7 depicts a microscope image of the fabricated chip. Each transmit channel has the additional option to use an external laser source that is coupled into the chip from auxiliary waveguides.

The device was characterized first in chip form using DC and RF probes. Due to space constraints a limited amount of DC and RF probes could be applied to the chip so that only one channel at a time was measured. The device was temperature controlled at 14.9 °C using a thermo-electric cooler and lensed single mode fibers are utilized to couple light in and out

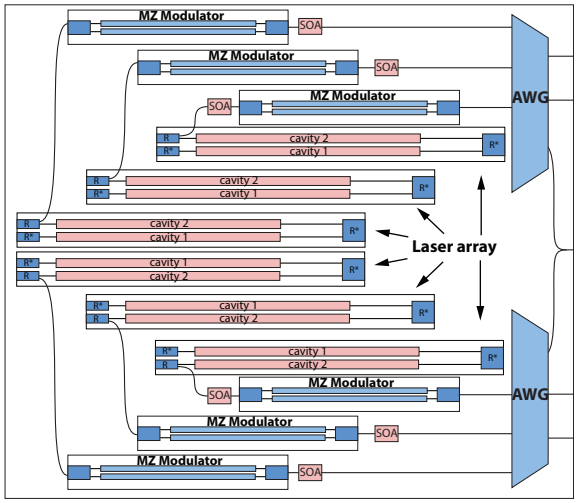

Fig. 6: Schematic diagram showing the layout of the six channel transmitter PIC, comprised of coupled-cavity lasers, SOA boosters, MZ modulators and passive AWG multiplexers.]

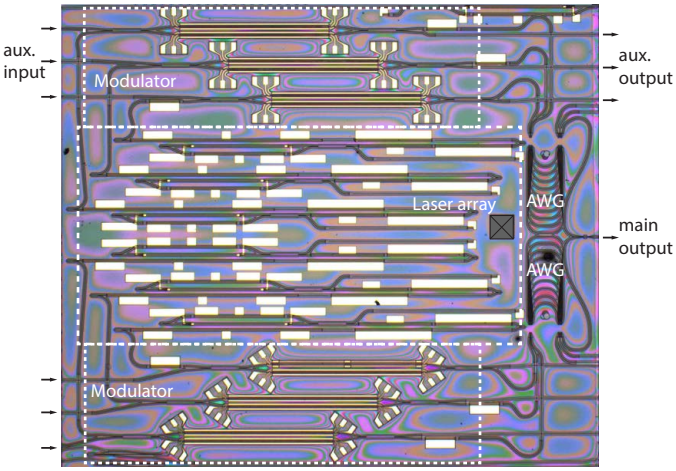

Fig. 7: Microscope image of the fabricated PIC, including auxiliary optical input and output ports.

of the chip. Fig. 8 shows the IV and LI curves of the six tunable lasers. Here, 125 mA was injected into the gain section of one cavity and the gain current of the second cavity is increased. We observe a threshold current around 15 mA, series resistance from 9 Ω to 13 Ω and maximum output power in fiber of around -10 dBm. Note here, that the values include the insertion loss of the modulators which is around 5 dB. Compared to the results in [17], thermal roll-off is less evident here and can be attributed to the offset introduced between the two gain sections. Jumps in the LI curve are caused by mode-hops that occur due to the increasing gain current and can be avoided in operation with proper tuning of phase sections of both cavities.

The booster SOAs can be used to increase the fiber-coupled power as Fig. 9 shows to -5 dBm with gain saturation occurring beyond 30 mA. It is placed after the modulator in four channels whereas the remaining two transmit channels have them implemented directly after the laser. The placement location has consequences on the stability of the laser. Fig. 10 shows the effect of the SOA on laser operation when

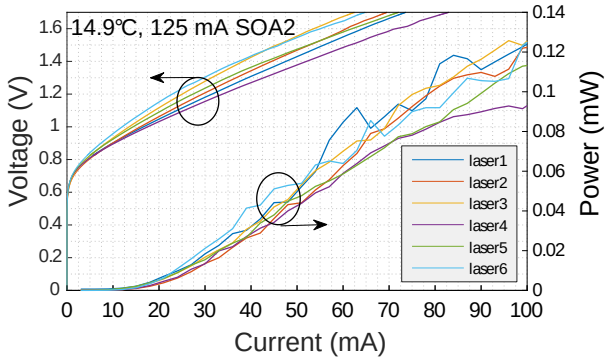

Fig. 8: Measured IV and LI curves of all six tunable lasers.

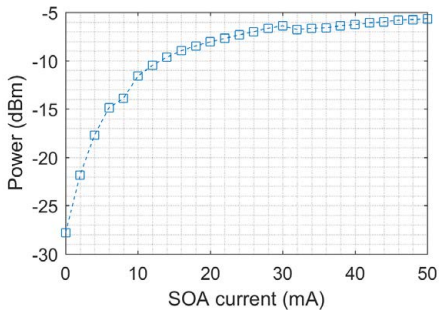

Fig. 9: Measured characteristic of the booster SOA with gain saturation occurring after 30 mA.

we measure the laser output from the auxiliary port for both configurations. The laser is not disturbed when placing the SOA after the modulator but is affected when the SOA is put directly after the laser, visible through mode hops in the spectrum. We think that spurious reflections from the modulator going back into the laser are amplified in the latter case, causing the disturbance of the lasing mode.

The modulator DC extinction is shown in Fig. 11 where the reverse bias voltage of one arm is swept and the optical

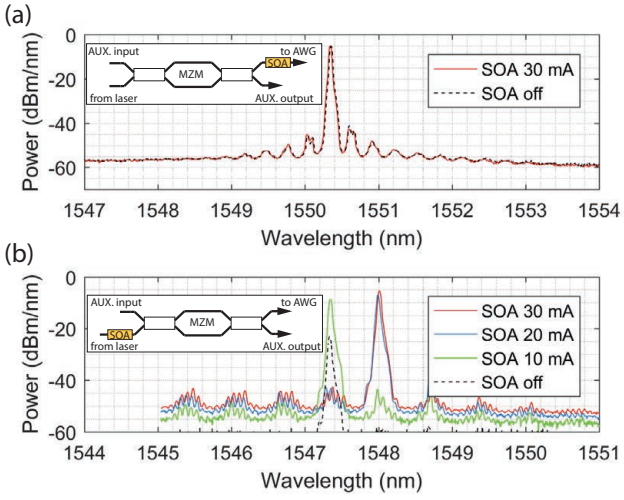

Fig. 10: The influence of SOA on laser spectrum is depicted in case (a) the SOA is placed after the modulator and in case (b) it is placed before the modulator. Measurement taken on aux. output.

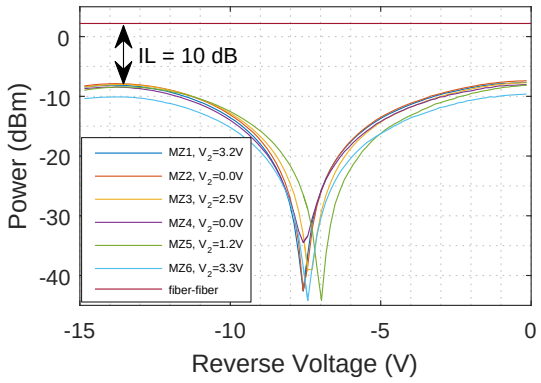

Fig. 11: DC switching curves of all six MZ modulators when compensated for initial phase offset. Insertion loss is measured against fiber-to-fiber reference level.

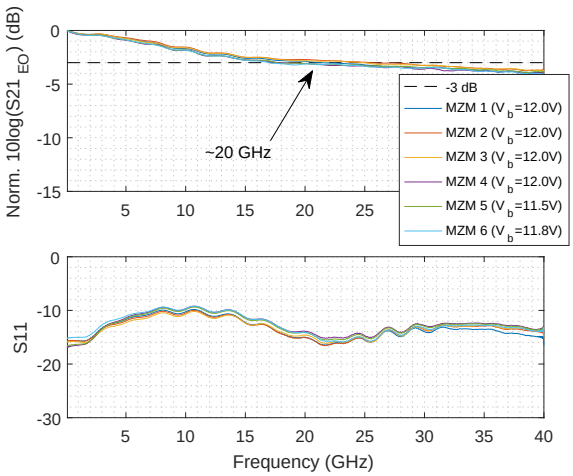

Fig. 12: Electro-optic S21 and S11 reflection measured for all six modulators with biasing at second quadrature point.

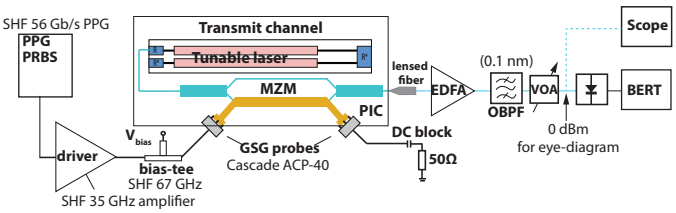

Fig. 13: Experimental setup for BER and eye diagram measurements. On-chip tunable lasers were used.

power transmission is measured through the auxilliary input and output waveguides with an external laser. The second arm of the modulator is biased to compensate for the initial phase offset between both arms. The launch polarization was adjusted to yield maximum phase-shift efficiency which corresponds to the TE polarization on chip, matching the output state of the integrated laser devices. The fiber-to-fiber coupled power is determined without device-under-test and acts as a reference level to calculate the modulator insertion loss. The total insertion loss of 10 dB includes the fiber-to-chip coupling losses of 2.5 dB on each side. A DC extinction >30 dB and a half-wave voltage just above 7 V can be obtained, yielding an efficiency of 9 Vmm.

The dynamic response of the modulators is characterized with an Agilent lightwave component analyzer (N4373C) after properly calibrating the reference plane to start at the RF probe tips. The obtained electro-optic S_{21} frequency response and electrical reflection S_{11} are shown in Fig. 12. A 3 dB bandwidth as defined in [27] of around 20 GHz is obtained with a worst-case reflection of -10 dB at 10 GHz, corresponding to an effective input impedance of 26 Ω, given the 50 Ω reference system. The frequency response rolls off gradually at higher frequencies, indicating potential to use the modulators also at high baud rates than is given by the 3 dB bandwidth.

To evaluate the performance under large-signal modulation, the integrated lasers are used to feed the modulators and eye diagrams are measured for each channel individually. The lasers are operated at their starting wavelength, as shown in Fig. 14, without additional tuning to reduce the probing complexity but can in practice be aimed to a wavelength of choice within the operation range following the strategy described in the previous section. The setup as shown in Fig. 13 is used where a PRBS $(2^{31}-1)$ pattern is generated, amplified and fed to the modulators via GSG probes. The bias voltage is applied through a broadband bias-tee and the output of the modulator electrode is terminated with a DC block and 50 Ω loads. Loads with 25 Ω would be a better match but were not readily available. The modulated optical output signal is amplified with an EDFA and bandpass filtered and adjusted to 0 dBm for eye diagram and bit error rate (BER) measurements. The results are shown in Fig. 15 and Fig. 16 for 20 Gb/s and 30 Gb/s NRZ modulation, respectively, and Fig. 17 contains the BER results. Clear eye openings and error-free operation are obtained at 20 Gb/s for all six channels. The eye diagrams at 30 Gb/s show increased closure and are effected more by intensity noise which we believe is caused by spurious reflections at interfaces between components or from the chip facet. Such reflections have been identified to increase noise in the modulation eye diagram [28]. In contrast, the shape of the eye transitions is not yet limited by the modulator bandwidth. BER above the HD-FEC limit is obtained, allowing in principle for 6 x 30 Gb/s operation.

PAM formats have gained popularity for short-reach applications recently as they exhibit increased spectral efficiency without the need for coherent detection and DSP. The modulators in this work show smooth EO response curves with a

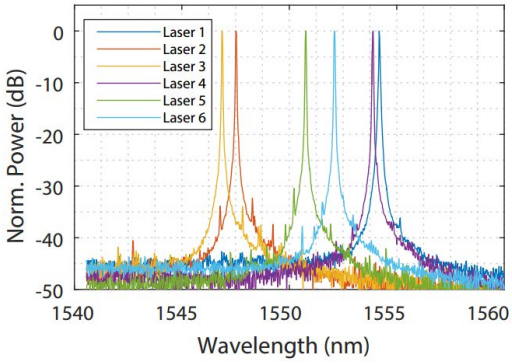

Fig. 14: Normalized spectra of the tunable lasers for eye diagram measurements of each channel. Wavelengths are kept at the starting position to reduce probing complexity.

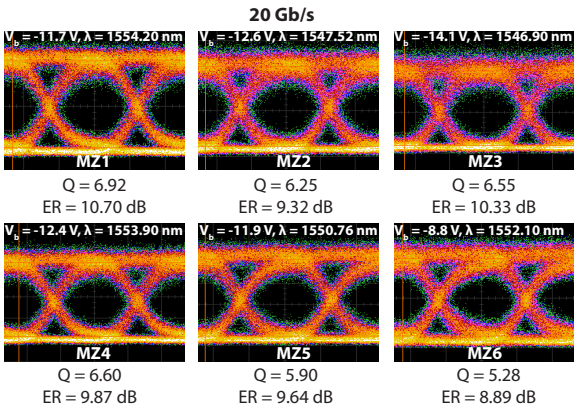

Fig. 15: Eye diagrams of all six channels at 20 Gb/s on-off keying.

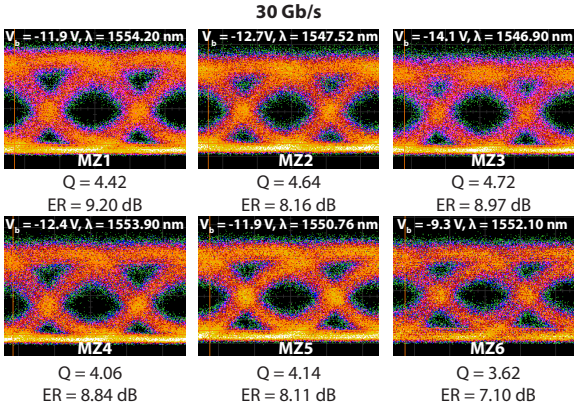

Fig. 16: Eye diagrams of all six channels at 30 Gb/s on-off keying.

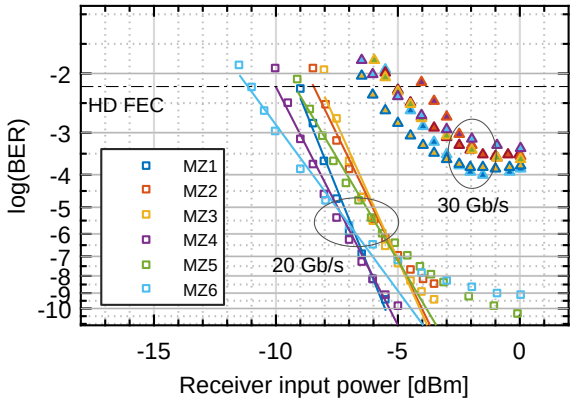

Fig. 17: Measured bit error rates at 20 and 30 Gb/s for all six channels.

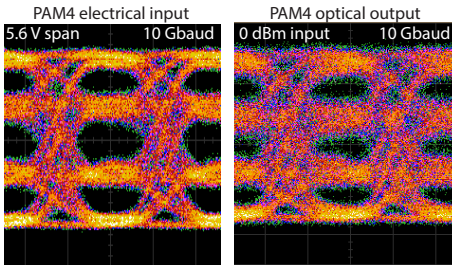

Fig. 18: Electrical PAM-4 drive signal and optical eye diagram of single-drive MZ modulator device.

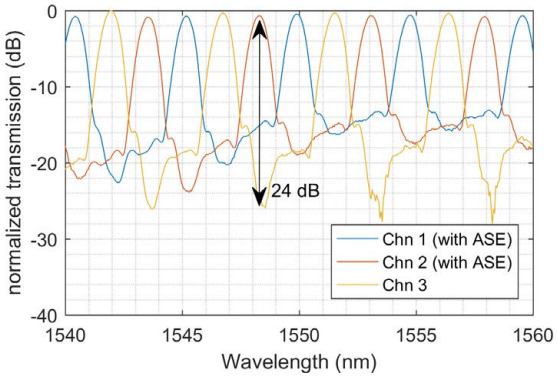

Fig. 19: Measured characteristic of the three channel AWG. Channel 1 and 2 include an SOA in the characterization path, which need to be biased for transparency, reducing the obtained dynamic range.

wide linear operation range and are therefore well suited for PAM-4 modulation. Fig. 18 depicts the 10 Gbaud eye diagram obtained on a test modulator with the same geometry as is used in the transmitter device. Driven with a PAM-4 electrical data signal, the modulator outputs a clear PAM-4 optical eye diagram. It can be observed that the limitation in this case is imposed by the poor electrical signal quality. As we have generated the electrical signal with analog attenuator and delay components, it was not possible to obtain BER measurements. It clearly shows the potential for the transmitter device to utilize multi-level modulation formats.

We have characterized the 3-channel AWG (200 GHz spacing, 600 GHz FSR) with the help of the auxiliary input and output ports and the results are shown in Fig. 19. Two of the three channels include a booster SOA in the measurement path that needs to be biased. This results in amplified spontaneous emission (ASE) noise, reducing the measured dynamic range of the AWG channel response. Channel 3 is not affected by this ASE noise and yields a crosstalk value of 24 dB. It was not possible to obtain the AWG insertion loss directly because it is embedded within the transmitter circuit. Similar AWGs fabricated in the same technology exhibit 3 dB insertion loss [29].

IV. Performance in Test Assembly

In case of densely integrated parallel transmitters crosstalk between channels can significantly degrade the device performance [14]. Especially radio-frequency (RF) crosstalk has

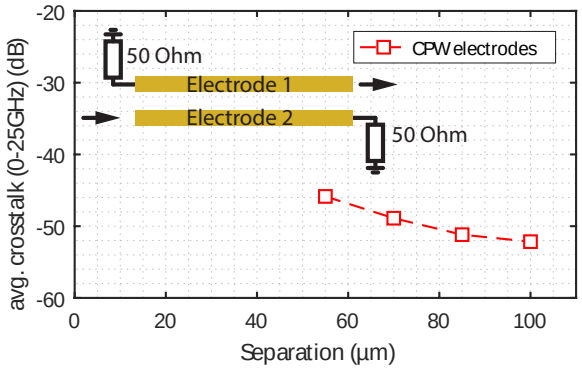

Fig. 20: Average crosstalk (0-25 GHz) as a function of electrode separation distance. Measured on modulator test structures from the same process.

been identified as one potential problem that introduces transmit power penalties to the system [30]. A viable way to reduce RF crosstalk is to separate ground return electrodes between channels and keep a minimum spatial distance between modulators [31]. In this device we utilize separate ground electrodes for all CPW transmission lines and keep the intra-modulator electrode distance to 70 μm and the inter-modulator distance to 220 μm. The former is chosen to exceed the minimum recommended distance for negligible RF crosstalk [31] whereas the latter is imposed by the size of the probing pads and not directly limited due to crosstalk. A further reduction of inter-modulator separation can be achieved if probing pads are omitted. We characterized the amount of crosstalk between the modulator electrodes as a function of their separation distance using test CPW lines (L = 1.15 mm). The results of the far-end crosstalk is averaged over a frequency span from 0 to 25 GHz and are shown in Fig. 20 where it can be seen that the chosen intra and inter modulator distances yield crosstalk at -50 dB and below, having negligible impact on the transmit performance.

In order to test the simultaneous operation of two or more channels, the transmitter device has to be embedded in a test assembly. A custom high-frequency printed-circuit board has been designed for this purpose, consisting of an array of RF and DC traces that lead to the chip edge where wire bonds are used to connect to the pads on the PIC. Fig. 21 depicts how the chip is interfaced with the PCB through which the bias signals for the lasers and also the RF drive, data and output terminations for the modulators can be applied. The high number of RF connections require a long fan-out section on the PCB so that its bandwidth is limited to 16 GHz as the simulation in Fig. 22 shows. Due to the small PIC size, the spacing of the PCB traces at the fan-in is reduced to its minimum with narrow ground guards. This causes a resonance behavior at multiples of 11 GHz, resulting in a rise in inter-channel crosstalk on the PCB, also clearly visible in Fig. 22. Apart from those resonant frequencies, the crosstalk is below -30 dB on the PCB.

Using the PCB assembly we operated two channels simultaneously where the second channel acts as a crosstalk aggressor source and compared the eye diagram and BER to the case where only a single channel is used. Fig. 23 shows the optical

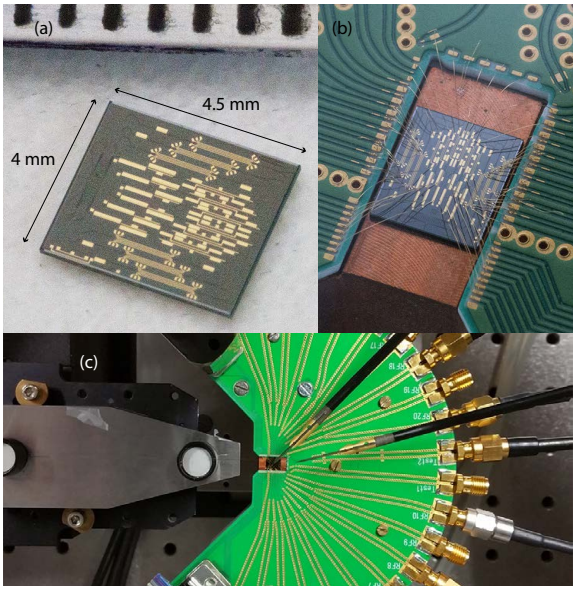

Fig. 21: Electrical printed-circuit board assembly with transmitter PIC, connected via wire bonds, to allow for multi-channel operation.

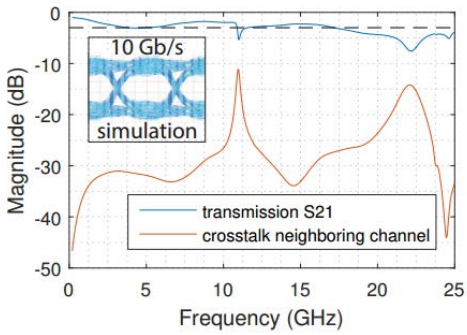

Fig. 22: Simulated electrical transmission and crosstalk of the printed-circuit board assembly.

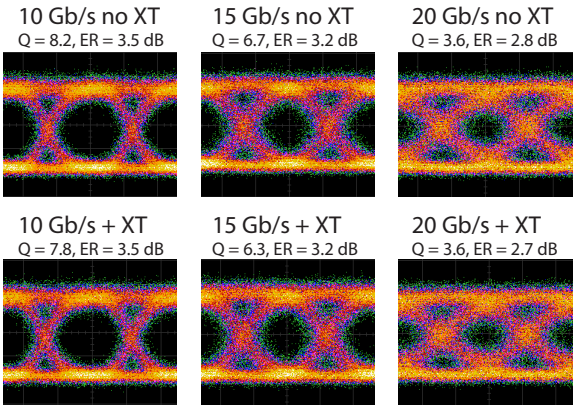

Fig. 23: Measured optical eye diagrams of the transmitter with and without neighboring crosstalk aggressor channel switched on.

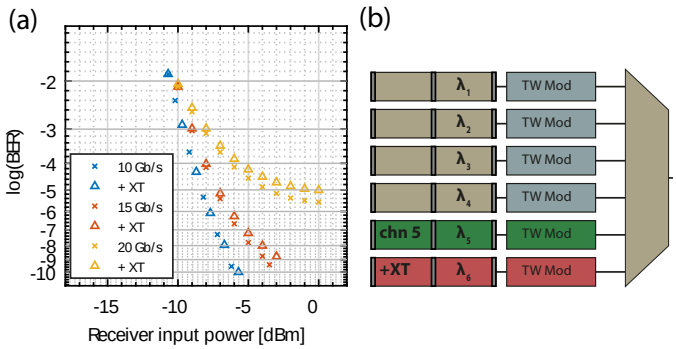

Fig. 24: Bit error rate of channel 5 with and without crosstalk aggressor.

eye diagrams in both cases for channel 5. The PCB assembly clearly limits the system bandwidth and only eyes until 20 Gb/s were obtained although the transmitter PIC has been shown to operate at higher speeds. No significant degradation of the eye pattern could be observed in presence of a crosstalk channel. This confirms that the PIC transmitter exhibits indeed low inter-channel RF crosstalk. The measured BER is shown in Fig. 24 for both cases. The crosstalk penalty is negligible at 10 Gb/s, grows to 1 dB at 10^{-9} BER for 15 Gb/s and 10^{-4} BER at 20 Gb/s. This can be attributed to the high crosstalk on the PCB at the mentioned resonance frequencies. We believe that an optimized assembly design would not cause any crosstalk penalty here. Note that the measured penalty value here is still lower than comparable work on a silicon transmitter [32].

Given the 200 GHz AWG spacing, enough guard distance is present to avoid optical crosstalk between channels at 30 Gb/s data rate. Furthermore, optical waveguides are placed >30 µm apart to avoid field coupling between them [33].

V. Discussions

This work shows a tunable parallel transmitter PIC from an open-access InP foundry platform based on a simple low-complexity integration process. With only one regrowth step and passive bulk waveguides widely tunable lasers with high-speed Mach-Zehnder modulators can be realized and monolithically integrated to form a high-density six-channel transmitter device. Such devices can be an attractive solutions for low-cost pluggable optics in gigabit ethernet or residential access networks. Presently, a foundry MPW is priced at 10000 USD, yielding 8 PICs with a total real estate of around 150 mm^2 [34]. This results in a price ratio of $\sim$70 USD/mm^2. Given a density metric of 10 Gb/s/mm^2 as outlined in table I for this WDM transmitter, it yields a price/capacity value of 7 USD/Gb/s, which is in the range of desired price levels for gigabit Ethernet applications [2].

A comparison of this work with recently published multi-channel transmitters shows several interesting aspects and is summarized in Table I. Except for [15] the other work was fabricated on platforms that are not open access and reference [32] was added to compare to recent silicon photonics technology. Recent work from Infinera [11] has been excluded in the table as it was not possible to estimate the metrics from the published information. It can be seen that, in general, more parallel channels in a chip results in a bigger chip area. Yet, the bandwidth density at chip edge metric remains in the range of 50 Gb/s/mm independent of the channel count. This is due to the nature of scaling parallel channels where the edge space increases linearly with channel count. The capacity density does vary among the chosen examples, where the device from [12] leads the metric due to the use of compact EAM modulators. This work exhibits the second largest capacity density value even though a low-complexity integration process is used. Furthermore, the advantage in this work lies in the wide tunability of each transmit channel, enabling flexible wavelength allocation. It should be noted however, that the low-complexity platform necessitates a more complex laser design with a bigger footprint compared to grating based tunable lasers. This is more sensitive to killer random defects and functional yield will be lower than that of more compact lasers in a production environment.

TABLE I: Comparison of this work with recent parallel transmitter PICs.

	this work	[14]	[15]	[32]	[12]
Technology	InP Tx (open access)	InP Tx	InP Tx (open access)	SiP TRx	InP Tx
year	2018	2018	2018	2018	2018
λ tuning (nm)	20 nm	7 nm	fixed array	fixed	30 nm
Data rate×chn	30 Gb/s×6	40 Gb/s×8	25 Gb/s×8	25 Gb/s×16	10 Gb/s×4
chip size (mm^2)	4×4.5	6×6	6×4	11×10	2×0.8 (estimated)
bandwidth density at edge (Gb/s/mm)	45	53	50	40	50
bandwidth density (Gb/s/mm^2)	10	8.9	8.3	3.6	25

The total power consumption of one transmit channel is around 700 mW resulting in 24 pJ/bit. The relative high power requirement is due to the bulk modulator material that requires large voltage swings and because the laser design uses two gain sections. If all channels are operated simultaneously, the temperature rise from resistive heating will induce wavelength changes and mode switching in the lasers. Those effects can be in principle compensated by tuning sections of the lasers, but in practice, are still challenging to manage and a sophisticated tuning strategy including the use of control electronics is needed.

Although the building blocks used in [14], [15] differ from each other, a very similar PIC functionality has been finally achieved on both platforms. The former utilizes tunable DBR lasers and Mach-Zehnder modulators whereas the latter employs directly modulated DFB lasers. In this work, each transmit channel is realized with coupled-cavity lasers together with Mach-Zehnder modulators, attributing again to the degree of functional interoperability among the InP foundries.

VI. Conclusion

In conclusion, we have presented detailed measurement results of a 6×30 Gb/s parallel tunable transmitter PIC, fabricated in a low-cost low-complexity open-access generic foundry platform. The device exhibits state-of-the-art 10 Gb/s/mm^2 capacity density metrics comparable to proprietary silicon and indium phosphide platforms, low < -50 dB RF inter-channel crosstalk between densely integrated modulators and 20 nm wavelength tunability. It shows low crosstalk

penalty between transmit channels and showcases the potential of the generic platform for future data center and access network applications at an attractive price level of 7 USD/Gb/s.

ACKNOWLEDGMENT

We acknowledge funding from the Dutch STW ELPHI project (11354) and the SMART Photonics foundry for chip fabrication. We thank Dr. D. D′Agostino and Dr. G. Gilardi for fruitful discussions.

REFERENCES

[1] "IEEE 802.3 100 Gb/s, 200 Gb/s, and 400 Gb/s Electrical Interfaces Task Force," http://www.ieee802.org/3/ck/index.html, IEEE Standardization Task Force.

[2] "Open Optics Multi Source Agreement," Open Compute Project, http://www.openopticsmsa.org/.

[3] Y. Luo, H. Roberts, K. Grobe *et al.*, "Physical Layer Aspects of NG-PON2 Standards—Part 2: System Design and Technology Feasibility [Invited]," *Journal of Optical Communications and Networking*, vol. 8, no. 1, p. 43, Jan. 2016.

[4] "G.989.2 : 40-Gigabit-capable passive optical networks 2 (NG-PON2): Physical media dependent (PMD) layer specification," https://www.itu.int/rec/T-REC-G.989.2-201412-I/en.

[5] K. Roberts, Q. Zhuge, I. Monga *et al.*, "Beyond 100 Gb/s: Capacity, flexibility, and network optimization [Invited]," *IEEE/OSA Journal of Optical Communications and Networking*, vol. 9, no. 4, pp. C12–C23, Apr. 2017.

[6] S. Pachnicke, J. Zhu, M. Lawin *et al.*, "Tunable WDM-PON System With Centralized Wavelength Control," *Journal of Lightwave Technology*, vol. 34, no. 2, pp. 812–818, Jan. 2016.

[7] K. Grobe, M. H. Eiselt, S. Pachnicke *et al.*, "Access Networks Based on Tunable Lasers," *Journal of Lightwave Technology*, vol. 32, no. 16, pp. 2815–2823, Aug. 2014.

[8] M. Smit, X. Leijtens, E. Bente *et al.*, "Generic foundry model for InP-based photonics," *IET Optoelectronics*, vol. 5, no. 5, pp. 187–194, 2011.

[9] M. Smit, X. Leijtens, H. Ambrosius *et al.*, "An introduction to InP-based generic integration technology," *Semicond. Sci. Technol.*, vol. 29, no. 8, p. 083001, 2014.

[10] A. Rahim, T. Spuesens, R. Baets *et al.*, "Open-Access Silicon Photonics: Current Status and Emerging Initiatives," *Proceedings of the IEEE*, vol. 106, no. 12, pp. 2313–2330, Dec. 2018.

[11] R. W. Going, M. Lauermann, R. Maher *et al.*, "1.00 (0.88) Tb/s per Wave Capable Coherent Multi-Channel Transmitter (Receiver) InP-Based PICs With Hybrid Integrated SiGe Electronics," *IEEE Journal of Quantum Electronics*, vol. 54, no. 4, pp. 1–10, Aug. 2018.

[12] D. J. Kebort, G. B. Morrison, H. Garrett *et al.*, "Monolithic Four-Channel (QUAD) Integrated Widely Tunable Transmitter in Indium Phosphide," *IEEE Journal of Selected Topics in Quantum Electronics*, vol. 24, no. 1, pp. 1–7, Jan. 2018.

[13] K. Lawniczuk, C. Kazmierski, J. G. Provost *et al.*, "InP-Based Photonic Multiwavelength Transmitter With DBR Laser Array," *IEEE Photonics Technology Letters*, vol. 25, no. 4, pp. 352–354, Feb. 2013.

[14] W. Yao, M. K. Smit, and M. J. Wale, "Monolithic 300 Gb/s Parallel Transmitter in InP-Based Generic Photonic Integration Technology," *IEEE Journal of Selected Topics in Quantum Electronics*, vol. 24, no. 1, pp. 1–11, Jan. 2018.

[15] N. Andriolli, P. Velha, M. Chiesa *et al.*, "A Directly Modulated Multi-wavelength Transmitter Monolithically Integrated on InP," *IEEE Journal of Selected Topics in Quantum Electronics*, vol. 24, no. 1, pp. 1–6, Jan. 2018.

[16] L. M. Augustin, R. Santos, E. den Haan *et al.*, "InP-Based Generic Foundry Platform for Photonic Integrated Circuits," *IEEE Journal of Selected Topics in Quantum Electronics*, vol. 24, no. 1, pp. 1–10, Jan. 2018.

[17] W. Yao, G. Gilardi, D. D'Agostino *et al.*, "Monolithic Tunable Coupled-Cavity WDM Transmitter in a Generic Foundry Platform," *IEEE Photonics Technology Letters*, vol. 29, no. 6, pp. 496–499, Mar. 2017.

[18] W. Yao, M. K. Smit, and M. J. Wale, "High-density monolithic 6 x 30 Gb/s tunable WDM transmitter in generic III-V platform," in *2017 Conference on Lasers and Electro-Optics Pacific Rim (CLEO-PR)*, Jul. 2017, pp. 1–2.

[19] F. A. Lemaitre, H. P. M. M. Ambrosius, J. Decobert *et al.*, "Implementation of the selective area growth in the COBRA generic photonic integration platform," in *Proceedings of the 20th Annual Symposium of the IEEE Photonics Benelux Chapter, 26-27 November 2015, Brussels, Belgium*. OPERA-photonics, Brussels School of Engineering, 2015, pp. 91–94.

[20] D. D'Agostino, D. Lenstra, H. Ambrosius *et al.*, "Widely tunable Coupled Cavity Laser based on a Michelson interferometer with doubled free spectral range," in *Optical Fiber Communications Conference and Exhibition (OFC), 2015*, Mar. 2015, p. M2D.4.

[21] ——, "Widely tunable multimode-interference based coupled cavity laser with integrated interferometer," *Optics Express*, vol. 26, no. 11, p. 14159, May 2018.

[22] D. D'Agostino, D. Lenstra, H. P. M. M. Ambrosius *et al.*, "Coupled cavity laser based on anti-resonant imaging via multimode interference," *Opt Lett*, vol. 40, no. 4, pp. 653–656, Feb. 2015.

[23] E. Kleijn, M. K. Smit, and X. J. M. Leijtens, "Multimode Interference Reflectors: A New Class of Components for Photonic Integrated Circuits," *J. Lightwave Technol., JLT*, vol. 31, no. 18, pp. 3055–3063, Sep. 2013.

[24] S. Irmscher, "Design, Fabrication and Analysis of InP-InGaAsP Traveling-Wave Electro-Absorption Modulators," PhD Dissertation, 2003.

[25] W. Yao, G. Gilardi, M. K. Smit *et al.*, "Equivalent circuit modelling of integrated traveling-wave optical modulator in InP foundry platform," in *18th European Conference on Integrated Optics (ECIO 2016), May 18-20, 2016, Warsaw, Poland*, May 2016, pp. 1–2.

[26] A. Mangan, S. Voinigescu, M.-T. Yang *et al.*, "De-embedding transmission line measurements for accurate modeling of IC designs," *IEEE Transactions on Electron Devices*, vol. 53, no. 2, pp. 235–241, 2006.

[27] "Keysight Technologies - High Speed Lightwave Component Analysis," application Note 5989-7808EN.

[28] C. Sun, B. Xiong, J. Wang *et al.*, "Influence of Residual Facet Reflection on the Eye-Diagram Performance of High-Speed Electroabsorption Modulated Lasers," *Journal of Lightwave Technology*, vol. 27, no. 15, pp. 2970–2976, Aug. 2009.

[29] J. Bolk, H. Ambrosius, P. Dasmahapatra *et al.*, "Ultra-low Loss Arrayed Waveguide Grating Using Deep UV Lithography on a Generic InP Photonic Integration Platform," in *2017 European Conference on Optical Communication (ECOC)*, Sep. 2017, pp. 1–3.

[30] W. Yao, G. Gilardi, N. Calabretta *et al.*, "Experimental and Numerical Study of Electrical Crosstalk in Photonic-Integrated Circuits," *Journal of Lightwave Technology*, vol. 33, no. 4, pp. 934–942, Feb. 2015.

[31] W. Yao, G. Gilardi, M. K. Smit *et al.*, "Performance Degradation of Integrated Optical Modulators Due to Electrical Crosstalk," *Journal of Lightwave Technology*, vol. 34, no. 13, pp. 3080–3086, Jul. 2016.

[32] T. Aoki, S. Sekiguchi, T. Simoyama *et al.*, "Low-Crosstalk Simultaneous 16-Channel x 25 Gb/s Operation of High-Density Silicon Photonics Optical Transceiver," *Journal of Lightwave Technology*, vol. 36, no. 5, pp. 1262–1267, Mar. 2018.

[33] D. Melati, F. Morichetti, G. G. Gentili *et al.*, "Optical radiative crosstalk in integrated photonic waveguides," *Opt. Lett.*, vol. 39, no. 13, pp. 3982–3985, Jul. 2014.

[34] "JePPIX," http://www.jeppix.eu/.

Weiming Yao received his B.Sc. degree in electrical engineering with honours from Technische Universität Berlin, Germany, in 2010, and graduated with two M.Sc. degrees in photonic networks engineering, with honours, as part of an Erasmus Mundus program from Aston University, Birmingham, UK, and Scuola Superiore Sant'Anna, Pisa, Italy, in 2012. Since then, he is with the Photonic Integration Group at Eindhoven University of Technology (TU/e) where his work focuses on the design and characterization of high bandwidth integrated multichannel transmitter PICs. He received his Ph.D. from Eindhoven University of Technology with honours in 2017.

Barry Smalbrugge received the Masters degree in solid state chemistry and inorganic chemistry from the Catholic University of Nijmegen (now Radboud University), Nijmegen, The Netherlands, in 1983, on subjects such as electroabsorption measurements at the indirect edge of silicon and electrochemical methods. He joined the Opto-Electronic Devices Group, Eindhoven University of Technology, Eindhoven, The Netherlands, in 1986. He is currently involved in back-end processing within IIIV semiconductor technology, wet-chemical etching, electrodeposition, scribing/cleaving, and wire-bonding.

Meint K. Smit graduated in Electrical Engineering in 1974 at the Delft University of Technology in the Netherlands and received his Ph.D. in 1991, both with honours. He started research in Integrated Optics in 1981 and is inventor of the Arrayed Waveguide Grating, for which he received a LEOS Technical Achievement award in 1997 and the Rank Prize in 2016. He was closely involved in the introduction of MMI-couplers in semiconductor based Photonic IC technology. From 2000 to 2014 he was the chair of the Photonic Integration group at the COBRA Research Institute of Eindhoven University of Technology. His current research interests are in InP-based photonic integration, including integration of InP circuitry on Silicon. He is the founder of the JePPIX platform, the Joint European Platform for Photonic Integration of Components and Circuits, and strongly involved in the development of the InP-based photonic foundry system in Europe. Meint Smit is an IEEE Photonics Society Fellow and received an ERC Advanced Grant in 2012.

Kevin Williams received the B.Eng. degree in electronic engineering from the University of Sheffield, Sheffield, U.K., and the Ph.D. degree in physics from the University of Bath, Bath, U.K., in 1995. His research interests include the area of integrated photonic circuits. He is the Chair of the Photonic Integration research group at Eindhoven University of Technology, Eindhoven, The Netherlands. He was awarded a Royal Society University research fellowship at the University of Bristol, Bristol, U.K, in 1996. He moved to the University of Cambridge, Cambridge, U.K., in 2001 and was elected a Fellow at Churchill College. In 2006, he was awarded a European Commission Marie Curie Chair at the Eindhoven University of Technology, The Netherlands. In 2011, he received the Vici Award from the Netherlands Organization for Scientific Research (NWO).

Michael J. Wale (M'92) received the B.A., M.A., and D.Phil. degrees in physics from the University of Oxford, U.K. He was the Director of Active Products Research at Oclaro Technology Ltd., based at Caswell, U.K. Since moving into industry in the early 1980s, he has been involved in many different aspects of research, development, and manufacturing of photonic devices and systems, with particular emphasis on photonic integrated circuit technology. Alongside his role at Oclaro, where he was responsibility for strategic technology activities, he is Professor of Photonic Integration/Industrial Aspects at Eindhoven University of Technology, The Netherlands, and an Honorary Professor at the University of Nottingham, U.K. He is a member of the Executive Board of the European Technology Platform, Photonics21, and the Chairman of its Working Group on Design and Manufacturing of Optical Components and Systems. He is a member of the Optical Society of America and is the author/co-author of approximately 200 publications.